# Fast Euler Solver for Transonic Airfoils Part II: Applications

Andrea Dadone*
*University of Bari, Bari, Italy*
and
Gino Morettit
*GMAF, Inc., Freeport, New York*

**The fast-solver code, described in Part I, is applied to compute several flowfields about a NACA 0012 airfoil at different Mach numbers and angles of attack. Some calculations are entirely subsonic and are used mostly to show convergence, symmetry, and accuracy of the code. Most results are for transonic flows. Effect of grid fineness and distance of the boundaries are analyzed. Comparison with other results is given. It is concluded that the code is indeed robust, accurate, and fast.**

## I. Introduction

THE computational technique for the analysis of steady, compressible, inviscid flows about airfoils, described in Ref. 1, is now applied to specific cases in order to prove its qualities. We focus our attention on NACA 0012 airfoils and consider several cases with wholly subsonic or transonic flows, with or without an angle of attack.

## II. Results for Subsonic Flows

With the program outlined in Ref. 1, subsonic flows about profiles of arbitrary shapes can be evaluated. We present some results obtained for a NACA 0012 airfoil: 1) with $M_\infty = 0.72$ and $\alpha = 0$ deg; and 2) with $M_\infty = 0.63$ and $\alpha = 2$ deg.

For both cases, we show plots of isomachs over the computed region; the distribution of $C_p$ over the airfoil; values of $C_L$, $C_D$, and $C_M$; a history of convergence; and an analysis of computational time (on a CRAY-XMP computer). An analysis of accuracy is also given for the first case. In all the present plots of $C_p$ over the airfoil, the correction discussed in Sec. IX of Part I has been applied to show what we consider a very close approximation to the real distribution of $C_p$ in the trailing edge region.

Figures 1 and 2 refer to the first case and have been obtained using the mesh that we consider the most appropriate for standard calculations (128 intervals in the $\xi$ direction and 32 intervals in the $\eta$ direction). In such a mesh, about 100 points lie on the surface of the airfoil.

Lift, drag, and moment coefficients (computed as explained in Sec. IX of Part I) are

$$C_L = 0(10^{-13}), \qquad C_D = 0.0008, \qquad C_M = 0(10^{-13})$$

The values obtained for the lift and moment coefficients show the perfect symmetry of the code. The low value of $C_D$ proves the efficiency of the technique outlined in Sec. IX of Part I. Comparison of the results presented in the figures with other results available in the literature[2] shows excellent agreement.

Figures 3 and 4 present similar results for the second case, obtained using the same mesh. Lift, drag, and moment coefficients are now

$$C_L = 0.3339, \qquad C_D = 0.00027, \qquad C_M = -0.0020$$

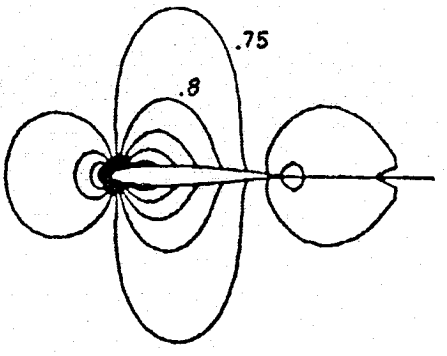


Fig. 1 Isomach pattern, $M_\infty = 0.72$, $\alpha = 0$ deg.

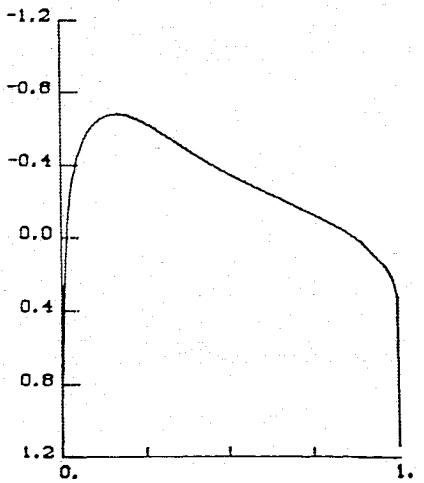


Fig. 2 $C_p$ distribution on airfoil, $M_\infty = 0.72$, $\alpha = 0$ deg.

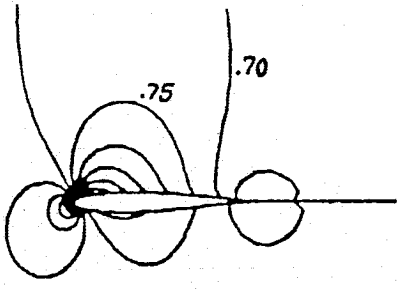


Fig. 3 Isomach pattern, $M_\infty = 0.63$, $\alpha = 2$ deg.

Received April 13, 1987; revision received Aug. 28, 1987. 

*Professor, Istituto di Macchine ed Energetica.

†Consultant. Fellow AIAA.

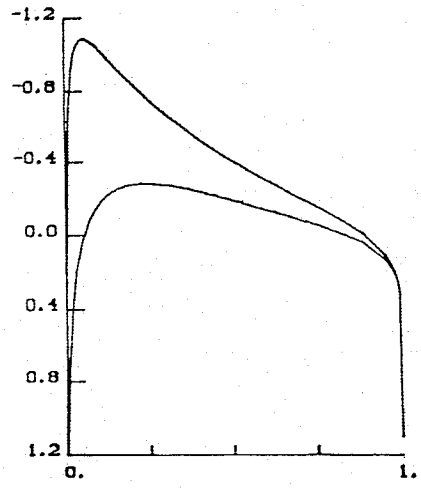


Fig. 4 $C_p$ distribution on airfoil, $M_\infty = 0.63$, $\alpha = 2$ deg.

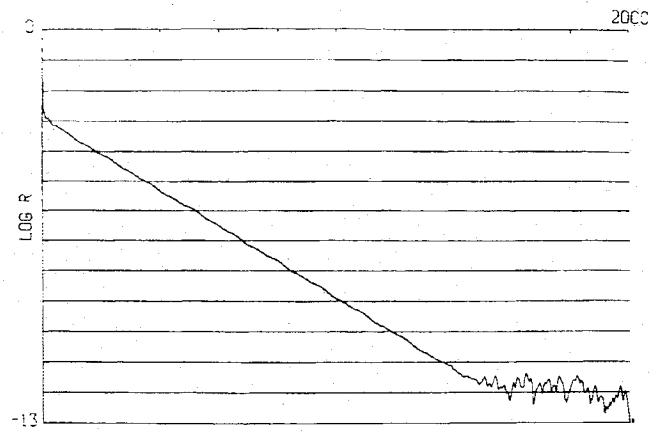


Fig. 5 Residual vs step number, $M_\infty = 0.72$, $\alpha = 0$ deg.

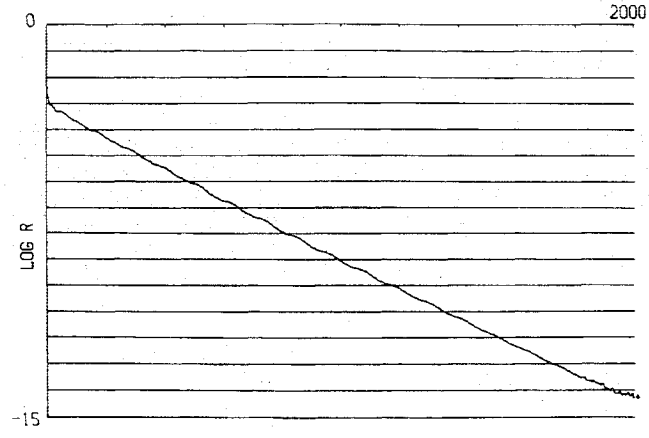


Fig. 6 Residual vs step number, $M_\infty = 0.63$, $\alpha = 2$ deg.

Once more, the comparison with the results of Ref. 2 is excellent; in particular, note that $C_L = 0.335$ in Ref. 2.

Speed of convergence and computational time (which are the focal points of interest in the present work) are analyzed as follows. Let $r$ be the mean square variation of the modulus of the velocity over the entire flowfield. We consider it a representative residual, and we have chosen it because of the sensitivity of the modulus of the velocity to errors. Values of the logarithm of $r$ (base 10) are plotted vs the step number (Figs. 5 and 6). For both cases and a $128 \times 32$ mesh, the residual reaches $10^{-12}$ in about 1500 steps.

The computational time is small. Here, we quote times needed on the CRAY-XMP to reach different convergence levels with different meshes

| | | $r = 10^{-6}$ | $r = 10^{-9}$ | $r = 10^{-11}$ |
|---|---|---|---|---|
| Case 1 | $128 \times 32$ | 5.0 s | 9.7 s | 13.0 s |
| | $64 \times 16$ | 0.6 s | 1.4 s | 2.0 s |
| | $32 \times 8$ | 0.1 s | 0.3 s | 0.4 s |
| Case 2 | $128 \times 32$ | 4.5 s | 9.5 s | 12.9 s |

It is to be noted that after the residual reaches $10^{-6}$, there is no practical change in the results and the calculation can be considered completed. We have continued the calculation simply to show that the residual keeps decreasing, i.e., the procedure converges.

An amazing result is obtained with the $32 \times 8$ mesh. A look at Figs. 7 and 8 shows that, even with a very coarse mesh (with only 27 points on the surface of the airfoil), the results are in pretty good agreement with the results obtained with the $128 \times 32$ mesh. Convergence history for this case is shown in Fig. 9.

Lift, drag, and moment coefficients are now

$$C_L = 0(10^{-13}), \qquad C_D = -0.0039, \qquad C_M = 0(10^{-14})$$

A closer inspection brings us to examine how the maximum Mach number and the minimum pressure coefficient on the body behave as functions of the fineness of the mesh. The analysis is shown in Fig. 10 where the maximum Mach number and the minimum pressure coefficient are plotted vs the square of the inverse of the total number of intervals in the $\xi$ direction.

Finally, in Figs. 11 and 12, we compare the decays of $r$ of the present code and of an explicit code working on the same grid for the same cases and using a local value of $\Delta t$, with a Courant number of 1 (the use of a local $\Delta t$, by itself, speeds up the convergence of the explicit code by one order of magnitude). The explicit code[3] integrates the equations as formulated by the $\lambda$-scheme, splitting each step into a

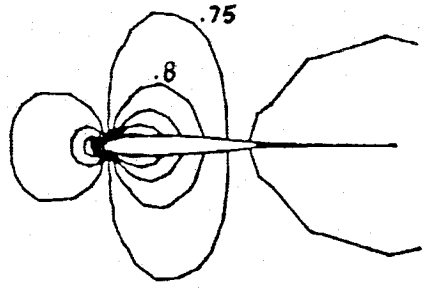


Fig. 7 Isomach pattern, $M_\infty = 0.72$, $\alpha = 0$ deg, $32 \times 8$ mesh.

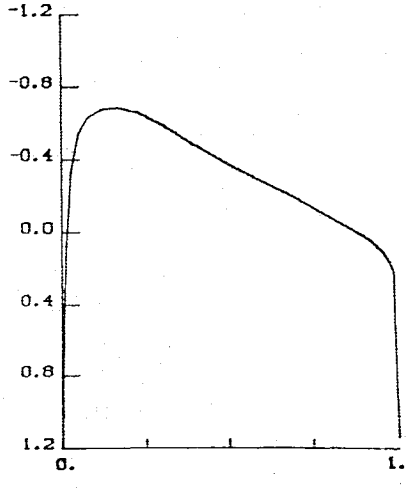


Fig. 8 $C_p$ distribution on airfoil, $M_\infty = 0.72$, $\alpha = 0$ deg, $32 \times 8$ mesh.

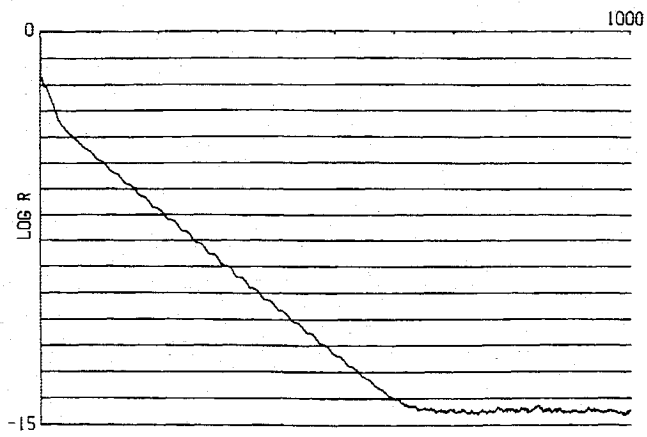


Fig. 9 Residual vs step number, $M_\infty = 0.72$, $\alpha = 0$ deg, $32 \times 8$ mesh.

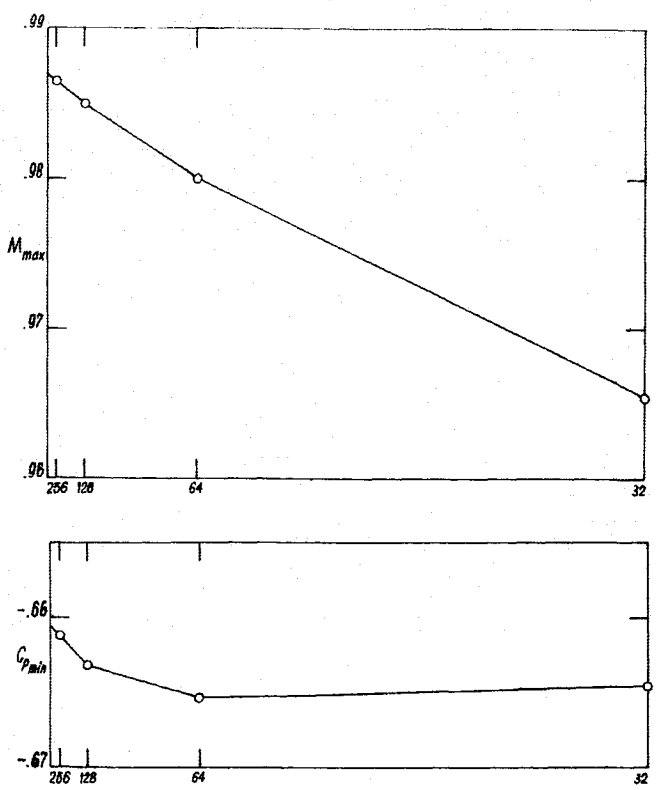


Fig. 10 Accuracy vs mesh fineness, $M_\infty = 0.72$, $\alpha = 0$ deg.

predictor level and a corrector level. To reach a value of $r$ of the order of $10^{-9}$, about 6500 (5500) steps are needed (all information in parentheses refers to the second case). No futher reduction in $r$ is possible; this is due to the use of a two-level scheme. To reach the same value of $r$, about 950 steps are needed with the present code, for both cases. The total computational time is 9 s for the present code and 116 s (98 s) for the explicit code; this represents a reduction by one order of magnitude.

## III. Results for Transonic Flows

We present results for the following four transonic cases, all obtained for a NACA 0012 airfoil using a $128 \times 32$ mesh:

1) with $M_\infty = 0.8$ and $\alpha = 0$ deg;
2) with $M_\infty = 0.85$ and $\alpha = 0$ deg;
3) with $M_\infty = 0.8$ and $\alpha = 1.25$ deg; and
4) with $M_\infty = 0.85$ and $\alpha = 1$ deg.

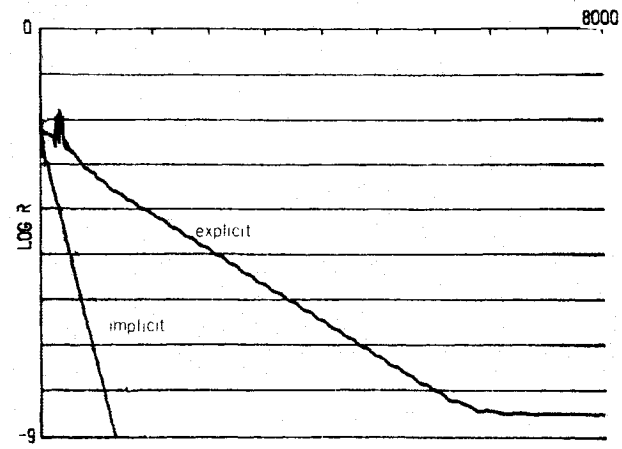


Fig. 11 Implicit vs explicit convergence, $M_\infty = 0.72$, $\alpha = 0$ deg.

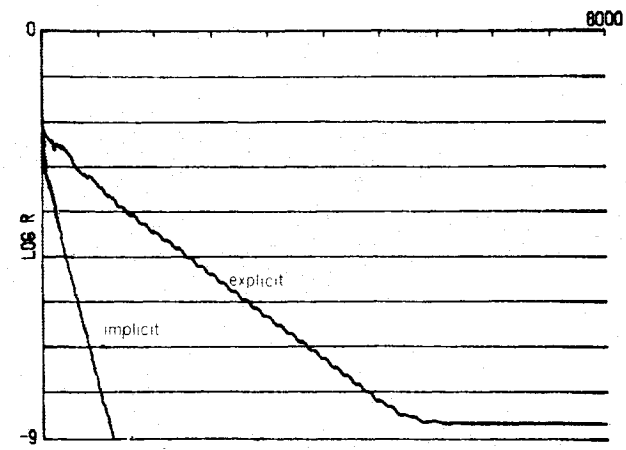


Fig. 12 Implicit vs explicit convergence, $M_\infty = 0.63$, $\alpha = 2$ deg.

For the first case, Figs. 13 and 14 show plots of isomach and isentropic lines over the computed region; the shocks are denoted by small crosses. Figure 15 presents the distribution of $C_p$ over the airfoil surface. Figures 16-21 present, for the other three cases, the same information as in Figs. 13 and 15.

The computed lift, drag, and moment coefficients are

| | $C_L$ | $C_D$ | $C_M$ |
|---|---|---|---|
| Case 1 | $0(10^{-10})$ | 0.0071 | $0(10^{-10})$ |
| Case 2 | $0(10^{-8})$ | 0.0431 | $0(10^{-9})$ |
| Case 3 | 0.375 | 0.0229 | −0.0399 |
| Case 4 | 0.361 | 0.0522 | −0.1186 |

The values obtained for the lift and moment coefficients in the nonlifting conditions (first two cases) show how well the code can preserve symmetry, both for subsonic and transonic flows.

The computed isomach patterns, $C_p$ distributions, aerodynamic coefficients, and shock positions compare very well with published results; see, e.g., Ref. 4 for the nonlifting cases and Refs. 5 and 6 for the lifting cases. The location of the shock, however, is defined with an accuracy that cannot be matched by shock-capturing codes.

In addition, the calculation is very fast; see in Figs. 22-25 the convergence histories of the four cases just given, and in the following display the times needed on the CRAY-XMP to reach certain levels of convergence:

| | $r = 10^{-6}$ | $r = 10^{-9}$ | $r = 10^{-11}$ |
|---|---|---|---|
| Case 1 | 7.7 s | 17.6 s | 24.4 s |
| Case 2 | 7.6 s | 16.8 s | 23.1 s |
| Case 3 | 12.2 s | 24.7 s | 33.8 s |
| Case 4 | 7.5 s | 17.6 s | 24.4 s |

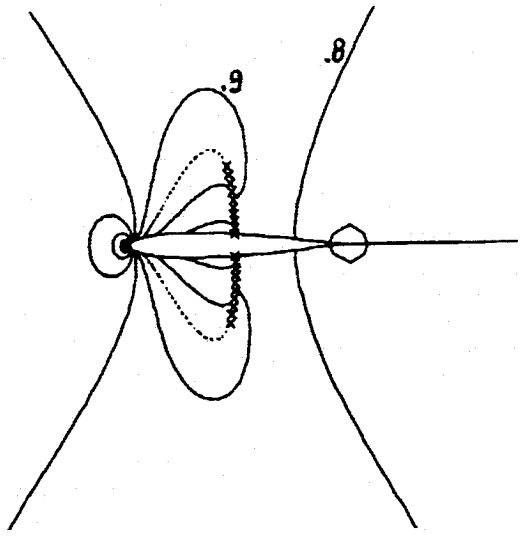


Fig. 13 Isomach pattern, $M_\infty = 0.80$, $\alpha = 0$ deg.

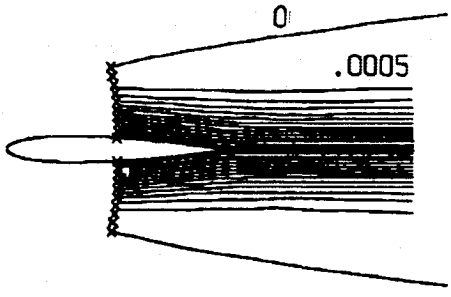


Fig. 14 Constant entropy lines, $M_\infty = 0.80$, $\alpha = 0$ deg.

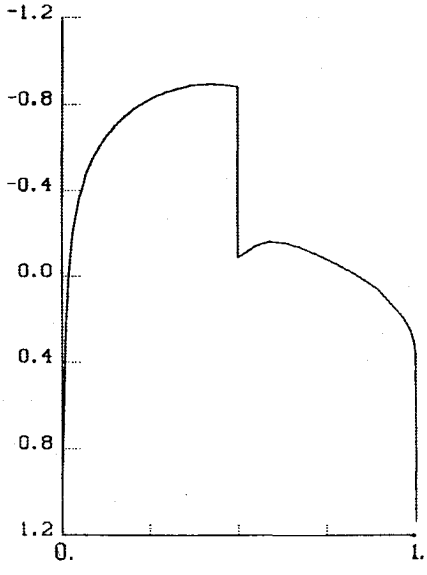


Fig. 15 $C_p$ distribution on airfoil, $M_\infty = 0.80$, $\alpha = 0$ deg.

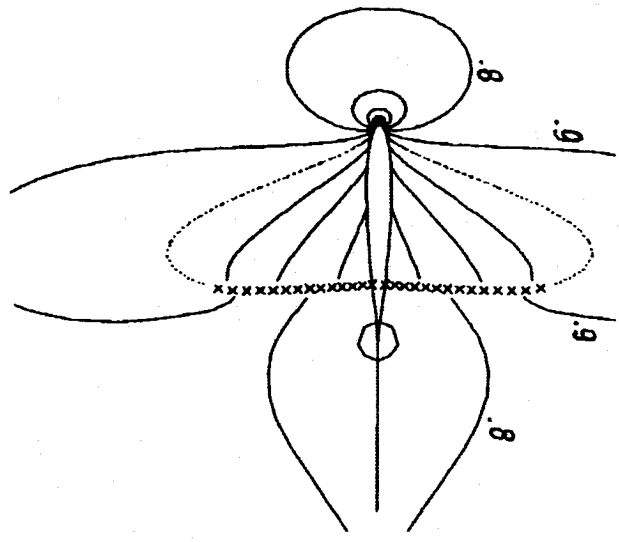


Fig. 16 Isomach pattern, $M_\infty = 0.85$, $\alpha = 0$ deg.

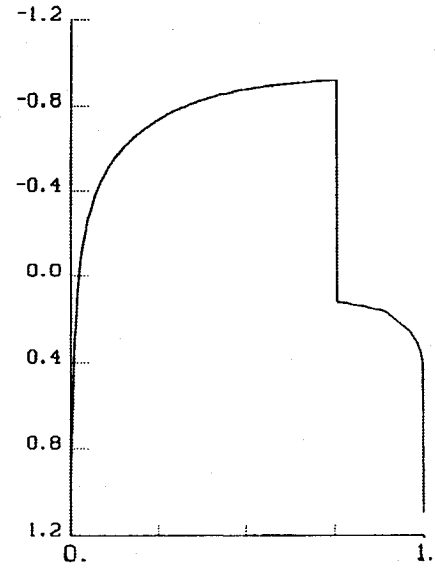


Fig. 17 $C_p$ distribution on airfoil, $M_\infty = 0.85$, $\alpha = 0$ deg.

The jagged form of the initial phases in Figs. 22–25 is due to the initial motion of the shocks. Once the shocks are settled in their final cells, the rate of convergence is practically constant.

Computational times are larger for transonic flows than subsonic flows. The increase is mostly due to more work to be done on the calculation of ordinary points (inversion of three-diagonal matrices, e.g.) and more iterations required to stabilize the shocks. The extra burden due to shock fitting, instead, is only 5–7% of the entire computational time.

Moreover, note that no result practically changes after the residual falls below $10^{-6}$, so that the calculation can be considered completed at this stage. This statement is substantiated by Fig. 26, which shows the evolution of the location of the shock root in all four cases, and by the following display, which gives the difference between the shock root locations at $r = 10^{-6}$ and $r =$ machine zero, in percents of the chord length:

| | |
|---|---|
| Case 1 | 0.06% |
| Case 2 | 0.03% |
| Case 3 | 0.016% |
| Case 4 | 0.005% (previously) and 0.022% (following) |

A direct comparison of convergence rates between the present calculation and similar transonic calculations with an explicit code[3] cannot be made yet. The explicit code lacks some important features that help the shock to freeze. As a consequence of minimal oscillations of the shock about its stable position, the values of $r$ oscillate up and down between

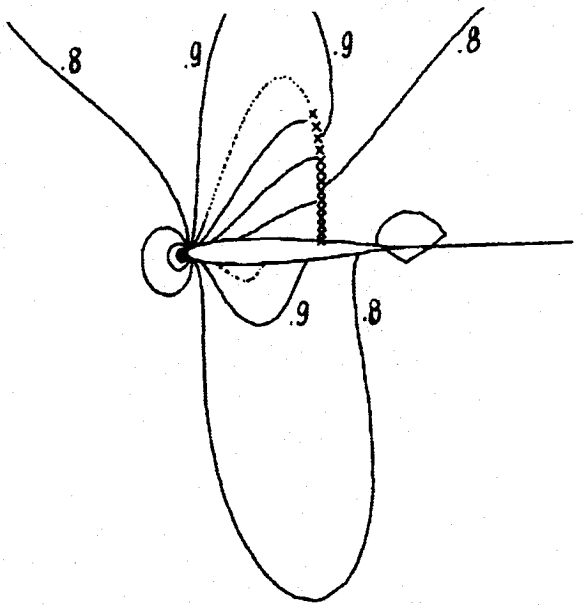


Fig. 18 Isomach pattern, $M_\infty = 0.80$, $\alpha = 1.25$ deg.

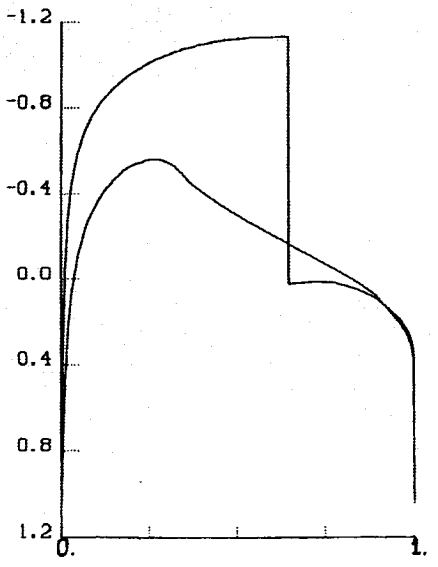


Fig. 19 $C_p$ distribution on airfoil, $M_\infty = 0.80$, $\alpha = 1.25$ deg.

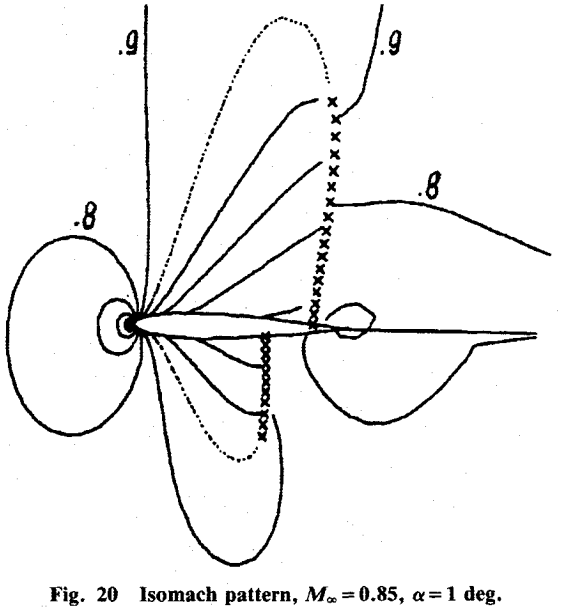


Fig. 20 Isomach pattern, $M_\infty = 0.85$, $\alpha = 1$ deg.

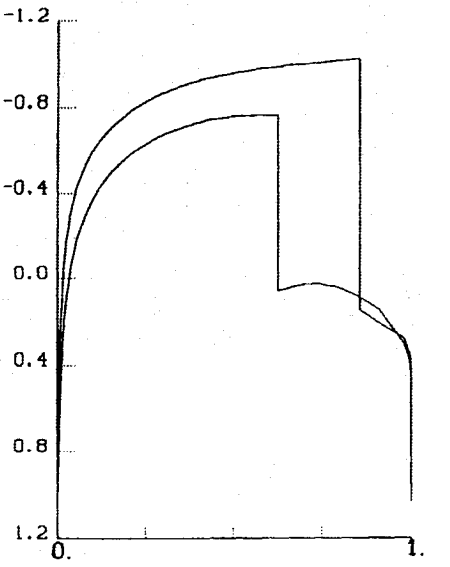


Fig. 21 $C_p$ distribution on airfoil, $M_\infty = 0.85$, $\alpha = 1$ deg.

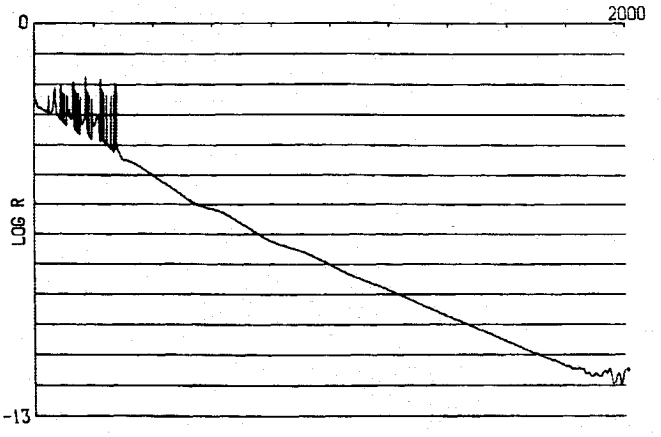


Fig. 22 Residual vs step number, $M_\infty = 0.80$, $\alpha = 0$ deg.

$10^{-6}$ and $10^{-4}$, e.g., making a diagram such as Fig. 22 meaningless.

We note that all the present calculations have been obtained without making use of multigrid devices. A further reduction in time by a factor of 2, at least, should be achievable with multigrids. We lack precise information on the computational speed of Jameson's code,[4] but we have good reasons to believe that our running times for practical convergence are comparable to Jameson's, and perhaps lower; in addition, we do not use multigrid devices. Comparison with any code based on flux-vector splitting or flux-difference splitting is definitively in our favor. According to Ref. 6, e.g., about 550 s (on the CRAY-XMP computer at the NASA Ames Research Center) are needed to reach the same level of convergence (with a $249 \times 41$ mesh) the present technique reaches in about 10 s (with a $128 \times 32$ mesh).

Finally, we would like to point out that, if a physical description of an unsteady evolution were needed, the present program could be used by simply replacing the local $\Delta t$ with a global $\Delta t$ and lowering the Courant number to 1.

To produce a transonic counterpart of Fig. 10, we show how the shock root location depends on the mesh, in case 1 (Fig. 27). The abscissas in Fig. 27 are the inverse of the total number of intervals in the $\xi$ direction. An amazing result is obtained, once more, using the $32 \times 8$ mesh. A look at Fig. 28 shows, indeed, that, even on a very coarse mesh, the results

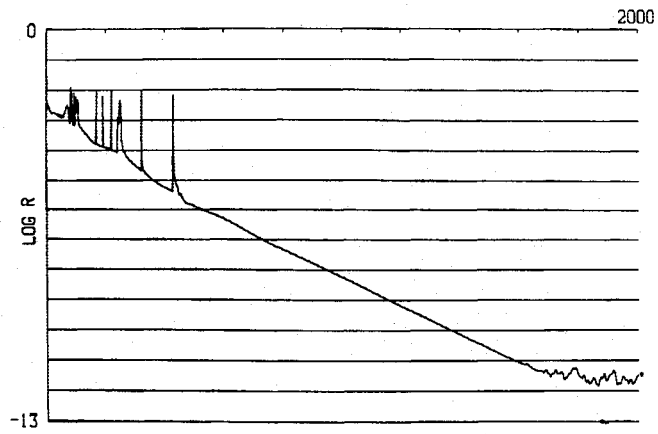


Fig. 23 Residual vs step number, $M_\infty = 0.85$, $\alpha = 0$ deg.

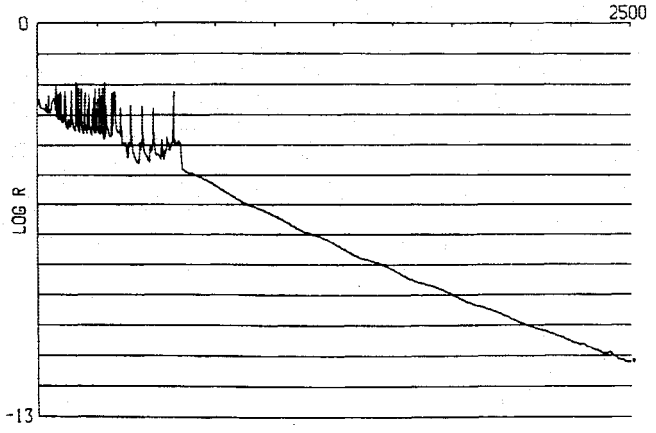


Fig. 24 Residual vs step number, $M_\infty = 0.80$, $\alpha = 1.25$ deg.

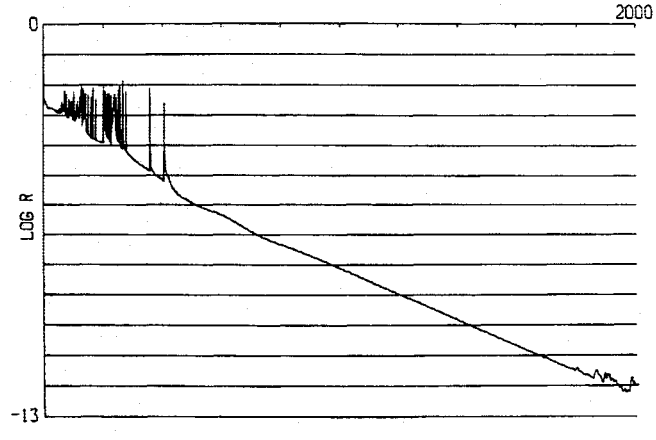


Fig. 25 Residual vs step number, $M_\infty = 0.85$, $\alpha = 1$ deg.

are in good qualitative agreement with those obtained with the $128 \times 32$ mesh. (Note that on the $32 \times 8$ mesh, only 27 points are located on the airfoil, most of which are concentrated near its leading edge.)

An important feature of the λ-scheme is its ability to handle boundary conditions; consequently, the boundaries can be set very close to the body. In all the calculations reported so far, the inlet and outlet boundaries were at a distance of 1.5 chord lengths from the leading and trailing edges, respectively. To evaluate the influence of the distance of the boundaries from the body, the first case has been recomputed after adding eight intervals in the $\eta$ direction, so that the inlet boundary moves to

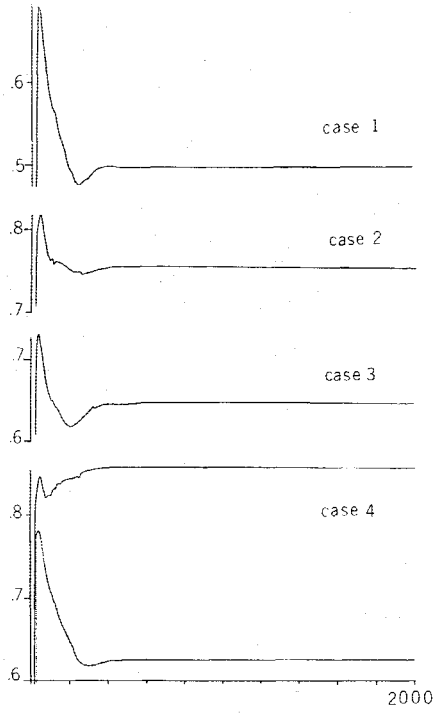


Fig. 26 Shock location on airfoil vs step number.

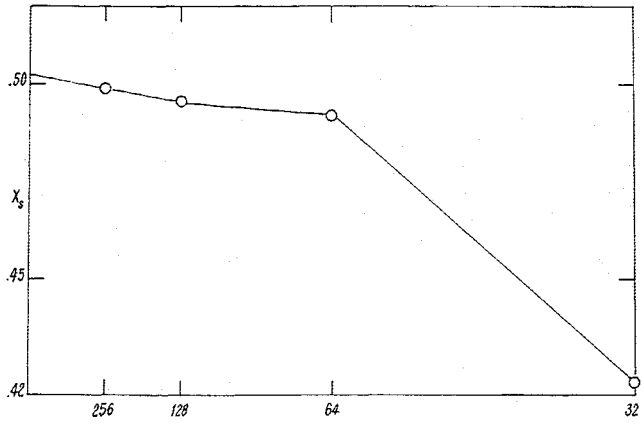


Fig. 27 Shock location accuracy vs mesh fineness, $M_\infty = 0.80$, $\alpha = 0$ deg.

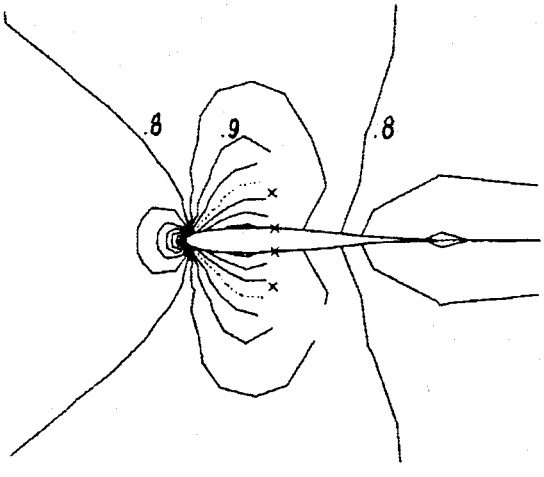


Fig. 28 Isomach pattern, $M_\infty = 0.80$, $\alpha = 0$ deg, $32 \times 8$ mesh.

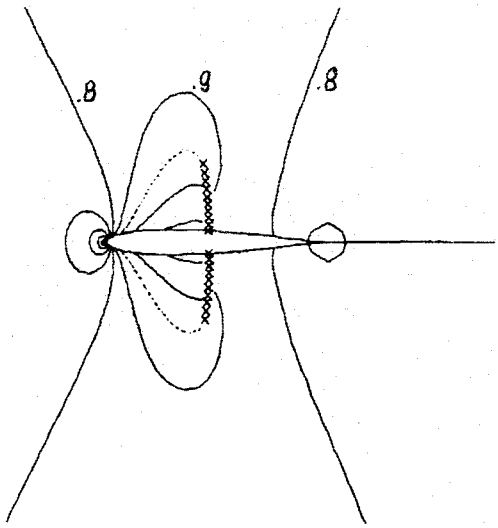


Fig. 29 Isomach pattern, $M_\infty = 0.80$, $\alpha = 0$ deg, $128 \times 40$ mesh.

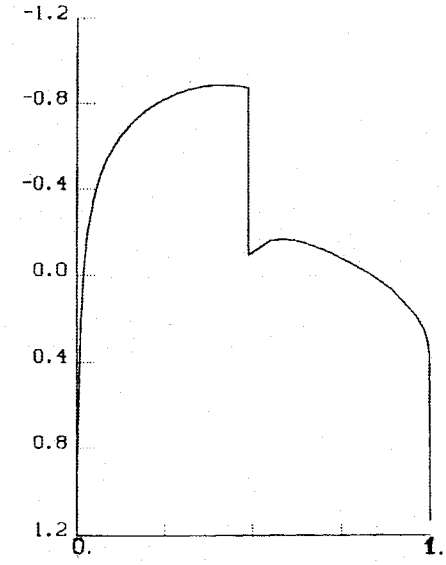


Fig. 32 $C_p$ distribution on airfoil, $M_\infty = 0.80$, $\alpha = 0$ deg, $136 \times 32$ mesh.

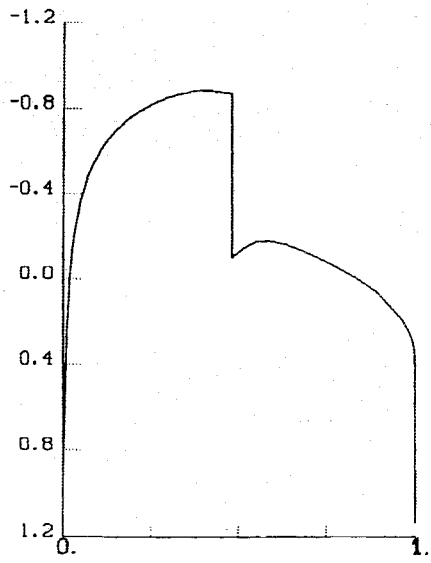


Fig. 30 $C_p$ distribution on airfoil, $M_\infty = 0.80$, $\alpha = 0$ deg, $128 \times 40$ mesh.

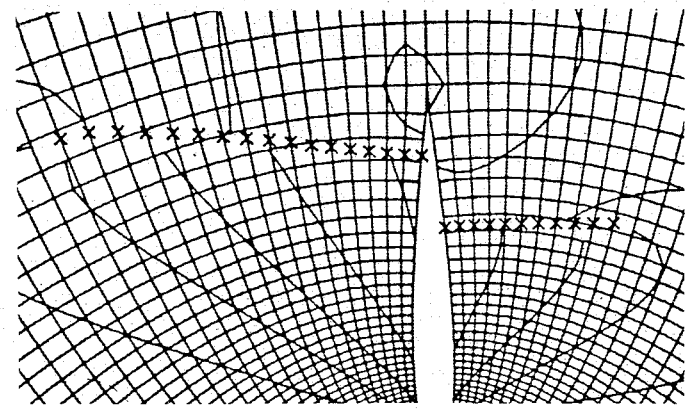

Fig. 33 Computational grid and fitted shocks, $M_\infty = 0.85$, $\alpha = 1$ deg.

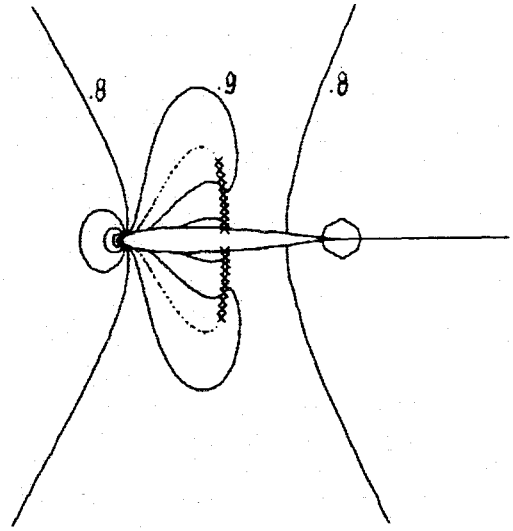


Fig. 31 Isomach pattern, $M_\infty = 0.80$, $\alpha = 0$ deg, $136 \times 32$ mesh.

3.2 chord lengths upstream. The corresponding plot of isomachs and the $C_p$ distribution on the airfoil are depicted in Figs. 29 and 30. Finally, the same case has been recomputed adding eight intervals in the $\xi$ direction, so that the outlet boundary moves to 3.6 chord lengths downstream. The corresponding results are shown in Figs. 31 and 32. A comparison of Figs. 13 and 15 with Figs. 29–32 prompts us to conclude that the influence of the location of the boundaries is remarkably small.

Last but not least, a nice feature of shock fitting, as applied in the present code, is the ability of the shock to cross grid lines (Fig. 33) without impairing accuracy and speed of convergence. In this respect, we are free from certain difficulties mentioned in Ref. 6 (a decrease in convergence rate when the shock is not aligned with the grid).

## IV. Conclusions

The aforementioned numerical applications and others that are not reported here prove that the technique described in Ref. 1 is fast and accurate. Specific advantages of the technique are the possibility of keeping the boundaries very close to the airfoil and the precision with which the shock location is defined. The latter differentiates the present technique from any other existing code. Ambiguities due to the spreading of the shock over two to five cells are eliminated; we consider this a step toward higher accuracy. Finally, no coefficients exist in

our code that need to be adjusted for fine tuning to assure or improve convergence.

## Acknowledgment

This research was carried out in 1986 under Contract NAS2-12355 from NASA Ames Research Center.

## References

[1]Dadone, A. and Moretti, G., "Fast Euler Solver for Transonic Airfoils, Part I: Theory," *AIAA Journal*, Vol. 26, April 1988, pp. 409-416.

[2]Lock, R. C., "Test Cases for Numerical Methods in Two-Dimensional Transonic Flows," AGARD Rept. 575, 1970.

[3]Moretti, G. and Lippolis, A., "Transonic Airfoil and Intake Calculations," GAMM Workshop, Rocquencourt, France, June 1986 (to be published in *Notes on Num. Fl. Mech.*, Vieweg, 1987).

[4]Jameson, A. and Yoon, S., "Multigrid solution of the Euler Equations Using Implicit Schemes," *AIAA Journal*, Vol. 24, Nov. 1986, pp. 1737-1743.

[5]Yoshihara, H. et al., "Test Cases for Inviscid Flow Field Methods," AGARD AR-211, 1985.

[6]Yee, H. C. and Harten, A., "Implicit TVD Schemes for Hyperbolic Conservation Laws in Curvilinear Coordinates," *AIAA Journal*, Vol. 25, Feb. 1987, pp. 266-274.